




 Cite this: *RSC Adv.*, 2022, 12, 2721

# Development of a ratiometric nitric oxide probe with baseline resolved emissions by an ESIPT and rhodol ring opened-closed integrated two-photon platform†

 Xumei Wang,<sup>a</sup> Qi Sun,<sup>a</sup> Xinjian Song,<sup>a</sup> \*<sup>a</sup> Yan Wang<sup>a</sup> and Wei Hu \*<sup>b</sup>

In recent years, reflecting the degree of cellular inflammation through *in situ* monitoring of nitric oxide using fluorescence sensing has received much attention due to many merits such as non-invasiveness and easy operation. In particular, two-photon excitation microscopy can significantly improve the imaging resolution and visualization time. In the meantime, a ratiometric-based nitric oxide fluorescent sensor can avoid the interference of many factors, including light source intensity, solvent scattering degree, solvent color, solvent viscosity, probe distribution, and instrument performance, and improve the accuracy of the result. However, the mutual interference of two emission peaks is still an issue restricting the development of this field. In this work, the Rh-NO-F dye obtained by modifying the rhodol dye with benzothiazole exhibited excited state intramolecular proton transfer (ESIPT) in the closed ring state. In the open ring state, however, the emission wavelength can be significantly red-shifted by increasing the degree of dye conjugation. By introducing *o*-phenylenediamine, the recognition domain of NO, we successfully designed and synthesized a ratiometric two-photon NO fluorescent probe, Rh-NO-P, which showed a 154 nm increase in the maximum emission wavelength before and after the response and almost no interference between the two emission peaks. Confocal imaging showed that the probe could achieve *in situ* detection of exogenous NO fluctuations in cells. The probe was also successfully applied to detect the changes in NO content during wound healing in mice.

 Received 17th November 2021  
 Accepted 22nd December 2021

DOI: 10.1039/d1ra08426g

[rsc.li/rsc-advances](https://rsc.li/rsc-advances)

## Introduction

As an important free radical in living organisms and an indispensable messenger molecule in pathological processes such as heart disease, immune system disease, and neurological degeneration disease, nitric oxide (NO) is produced from L-arginine under the action of nitric oxide synthase.<sup>1–5</sup> Revealing the distribution and concentration fluctuations of NO is essential for the early diagnosis of the above-mentioned diseases.<sup>6–10</sup>

Currently, fluorescence imaging has provided powerful assistance for real-time and *in situ* detection of NO distribution and concentration fluctuations in living organisms due to its advantages of simple operation, visualization, high sensitivity, and high spatial and temporal resolution. A large number of NO

fluorescent probes have been developed, which mainly include organic fluorescent probes and metal–ligand complex probes.<sup>11–15</sup> However, due to the limitation of the response mechanism, most NO probes exhibit the characteristics of a turn-on or turn-off type, and ratiometric fluorescent probes are rarely reported.<sup>16–20</sup> It is known that ratiometric fluorescent probes can correct the two emission peaks by themselves to eliminate the effects of environmental factors on the experimental results (including artificial interference caused by the environmental change of the probe, probe concentration, and excitation intensity) and increase the effective range of the fluorescence measurement.<sup>21–26</sup> Based on FRET scaffold carrying BODIPY and TMR fluorescent beams, Xiao's group reported a ratiometric fluorescent probe with high sensitivity and selectivity to NO, which was the pioneering work in this field.<sup>27</sup> After that, NO sensitivity ratiometric fluorescent probes have been continuously reported.<sup>28</sup> However, the crosstalk interference between the two emission peaks seriously affects the accuracy and resolution of the results. Therefore, expanding the distance while reducing the interference between the two emission peaks and effectively improving the accuracy and resolution of ratiometric fluorescent probes remains one of the scientific problems requiring urgent solutions.

<sup>a</sup>Hubei Key Laboratory of Biological Resources Protection and Utilization, School of Chemical and Environmental Engineering, Hubei Minzu University, Enshi, 445000, China. E-mail: whxjsong@163.com

<sup>b</sup>College of Bioresources and Materials Engineering, Shaanxi University of Science & Technology, Xi'an, 710021, China. E-mail: huwchem@sust.edu.cn

† Electronic supplementary information (ESI) available: Experimental details and characterization of Rh-NO-F and Rh-NO-P supplementary spectral results. See DOI: 10.1039/d1ra08426g



The current strategies for constructing ratiometric fluorescent probes mainly include the charge transfer mechanism (ICT, including intramolecular electron transfer and twisted intramolecular charge transfer),<sup>29</sup> excited state intramolecular proton transfer (ESIPT), and energy transfer (including fluorescence resonance energy transfer and through-bond energy transfer).<sup>30,31</sup> The charge transfer mechanism and excited state proton transfer are based on changing the energy difference between the highest occupied molecular orbital (HOMO) and the lowest unoccupied molecular orbital (LUMO) of the molecule, which could lead to synchronous changes in the emission wavelength and the absorption wavelength before and after the response. The complete separation of the two emission peaks requires two different excitation wavelengths, which will result in more cumbersome detection procedures and unguaranteed accuracy. In recent years, ratiometric fluorescent probes constructed based on energy transfer, especially through-bond energy transfer, have been reported by our group to have single-wavelength excitation and dual-emission peaks baseline separation. However, the large molecular weight and high fat solubility limit the probes' high sensitivity real-time target monitoring in living organisms.

Our group previously reported a fluorescent dye **Rh-NO-F** based on the rhodol dye, which exhibited excellent photophysical properties of the rhodol dye, such as high fluorescence quantum yield, large molar absorption coefficient, and good light stability, but also extended the  $\pi$ -conjugated system of the rhodol fluorescent dye through the introduction of the strong electron-withdrawing group 2-(2-hydroxyphenyl)-benzothiazole (HBT), thereby ensuring that the emission wavelength reached the near-infrared region.<sup>32–34</sup> In this work, **Rh-NO-F** was modified with *o*-phenylenediamine (**Rh-NO-P**), a typical NO recognition domain, to close its ring, thereby quenching the fluorescence emission of the rhodol dye. Thus, the free state hydroxyl group can undergo an excited state intramolecular proton transfer with HBT to emit shorter-wavelength fluorescence. What's more, regardless of whether excitation in one-photon mode (380 nm) or two-photon mode (800 nm), two non-interfering fluorescence emission peaks (with emission wavelengths of 457 nm and 611 nm) appeared before and after the reaction between **Rh-NO-P** and NO, which had a distance of 154 nm. *In vitro* experiments showed that **Rh-NO-P** had a highly sensitive response to NO with a detection limit of 51.3 nM, and its ratio intensity reached the maximum at 20 s, which was enhanced approximately 110.9-fold. In the end, we used NO as an inflammation marker and successfully tracked the fluctuations in the degree of cellular inflammation during wound healing in mice.

## Results and discussion

### Preparation and photophysical properties of Rh-NO-P

Two emission peaks without crosstalk are very important for further improvement of sensitivity and resolution. The construction of a proportional sensing system with two separate emission bands by spiro ring opening and excited state intramolecular proton transfer (ESIPT) has been reported. We

combined the rhodol open-closed loop and ESIPT mechanism to develop a proportional probe that completely separates the two emission peaks. Due to the excellent optical and physical properties of rhodol dye with a typical D- $\pi$ -A structure, including high fluorescence quantum yield, large molar absorption coefficient, good light stability, *etc.*, it attracts extensive attention in the construction of various fluorescent probes and biological simulations.<sup>35–37</sup> In addition, rhodol dye modified with benzothiazole (named **Rh-NO-F**) can take advantage of benzothiazole to increase the electron-withdrawing ability and the  $\pi$ -conjugate extension ability of the fluorescent parent molecule to improve the emission wavelength and two-photon activity cross-section of rhodol. More importantly, in this study, **Rh-NO-F** was modified with *o*-phenylenediamine (**Rh-NO-P**), a typical NO recognition domain, to close its ring, thereby quenching the fluorescence emission of the rhodol dye. Since the free state hydroxyl group could undergo an ESIPT with benzothiazole, short-wavelength blue fluorescence was emitted. When the probe **Rh-NO-P** interacted with NO, the recognition unit *o*-phenylenediamine left, and **Rh-NO-F** was in an open-loop state. Additionally, the rearrangement of electrons in rhodol caused the hydroxyl group to be converted into a more stable ketone carbonyl group so that the ESIPT effect disappeared, and the system produced red fluorescence. The probe showed a ratio emission peak without crosstalk in response to NO, which contributed to the improvement of the sensitivity and resolution in biological imaging. Based on the aforementioned strategy, **Rh-NO-P** was successfully synthesized. The synthetic routes and characterization details are shown in Fig. 1a and S1–S3.†

Based on the above analysis, this study first detected the photophysical properties of the fluorophore **Rh-NO-F** in different solvents. As shown in Fig. S4 and Table S1,† **Rh-NO-F** has two obvious absorption peaks in different solvents at 350 nm and 560 nm, and the maximum emission peak appears at 580–590 nm. The polarity of the solvent has a negligible influence on the emission wavelength and quantum yield of **Rh-NO-F**. Meanwhile, **Rh-NO-F** shows the highest quantum yield in dimethyl sulfoxide (DMSO,  $\Phi = 0.61$ , rhodamine B as a reference). Therefore, in all the following experiments, we used PBS buffer containing DMSO as the measurement conditions. Next, the solubility of **Rh-NO-P** was determined under the conditions of PBS buffer (10 mM, pH = 7.4, containing 10% DMSO). The results are shown in Fig. S5.† The absorption spectroscopy shows that when the concentration of **Rh-NO-P** reaches 25  $\mu$ M, the intensity does not reach the plateau, indicating that the probe still has good solubility and therefore it can be used for detection in subsequent experiments. Then, the absorption and emission spectra before and after the reaction of **Rh-NO-P** with NO were investigated. It can be seen from Fig. 1c and d that **Rh-NO-P** itself has an obvious absorption peak at 360 nm, and the fluorescence emission occurs at 457 nm. However, after the reaction with NO, the absorbance at 360 nm increases slightly, and a new peak occurs at 560 nm. In addition, the fluorescence emission peak moves from 457 nm to 611 nm after the response. The possible reason for this movement is that the probe reacts with NO to produce the triazole derivative

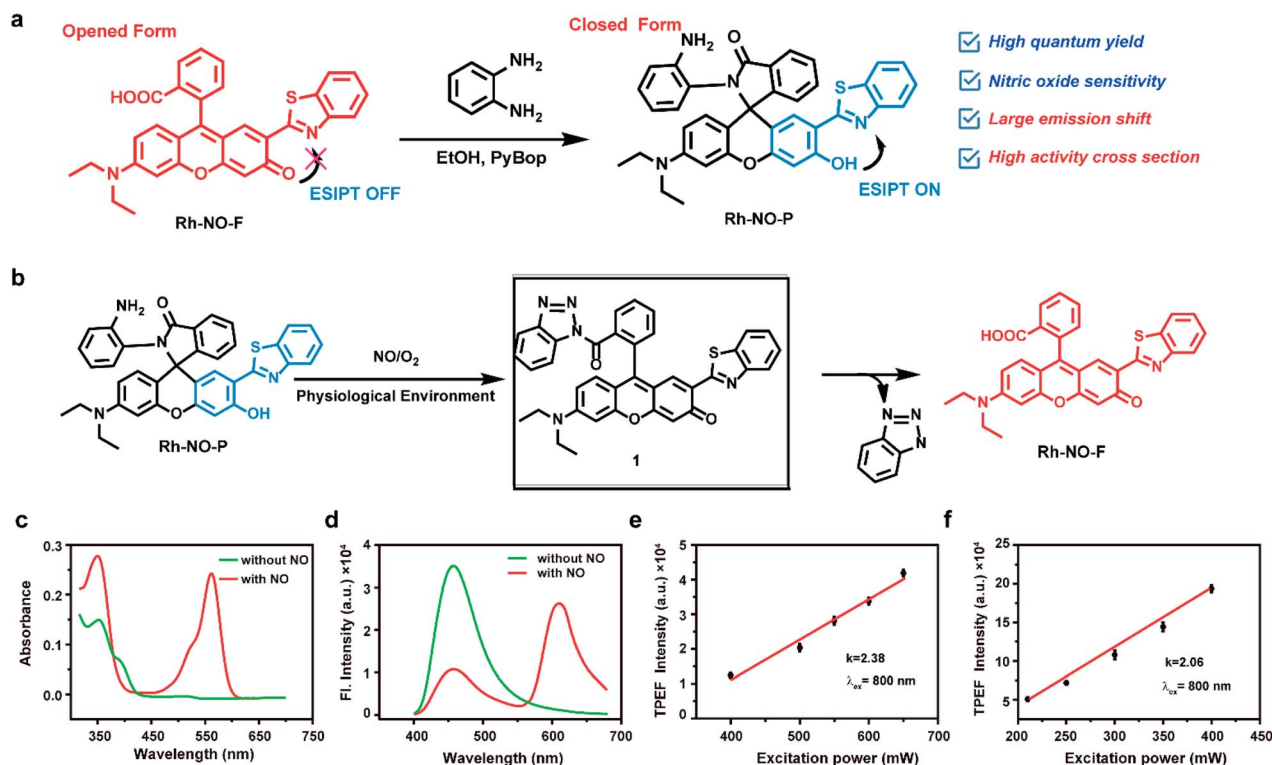
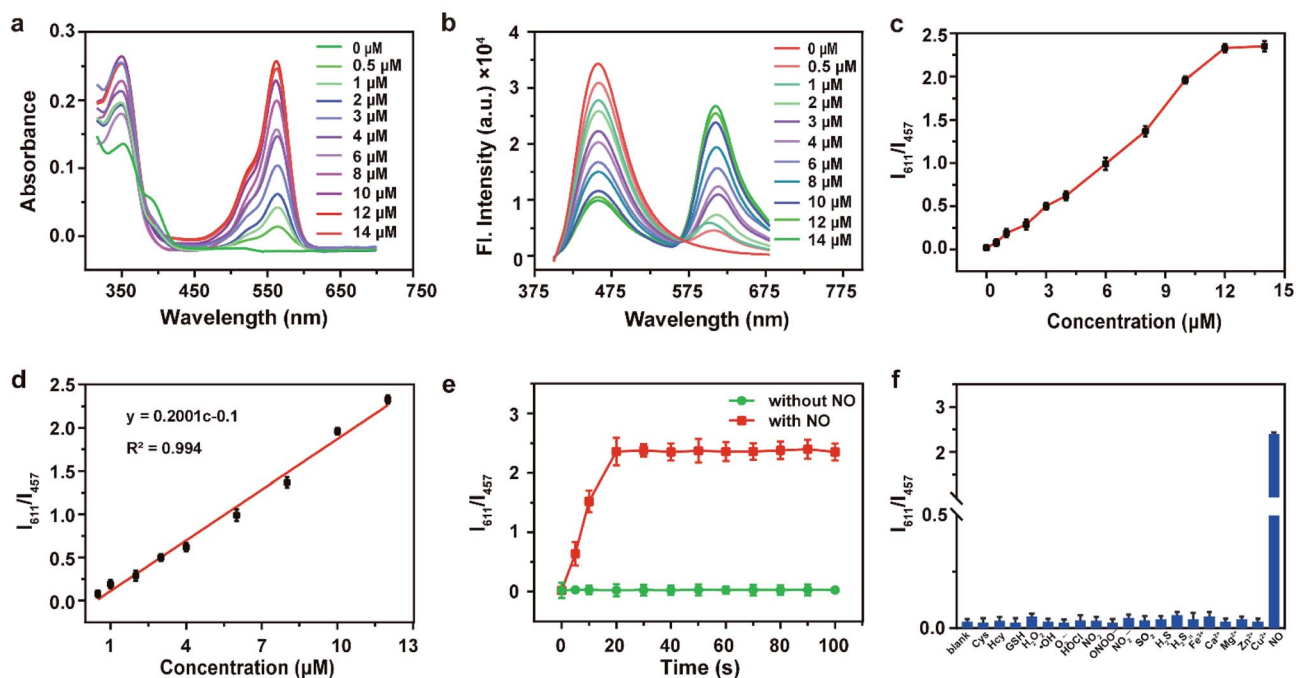


Fig. 1 (a) Chemical structures and synthetic route of Rh-NO-P. (b) Mechanism and pathway of probe Rh-NO-P for NO. (c) Absorption spectra and (d) fluorescence spectra of Rh-NO-P with (red line) or without (green line) NO. Logarithmic plots of the dependence of fluorescence intensity on excitation power for Rh-NO-P without (e) and (f) with NO. In (e) and (f), data represent the mean of three replicates, and the error bars indicate the SD. Concentration of Rh-NO-P: 10  $\mu\text{M}$ .

intermediate 1; then benzotriazole is hydrolyzed and falls off to form the fluorophore **Rh-NO-F**; the ESIP effect disappears, and the opening of the rhodamine ring occurs (shown in Fig. 1b). In order to verify the speculation of the response mechanism of probe **Rh-NO-P** and NO, HR-MS was applied (see the ESI, Fig. S6†). It can be seen that the molecular ion peaks of **Rh-NO-P**, 1 and Rh-NO-F are 611.2089, 622.1831, and 521.1452, respectively, which proves the rationality of the speculation. In order to evaluate whether the probe **Rh-NO-P** can be used for two-photon confocal imaging, this work investigated the relationship between two-photon emission intensity and excitation optical power. The results indicated that the slopes of the square of the two-photon excitation optical power *versus* the two-photon fluorescence intensity of **Rh-NO-P** and **Rh-NO-F** are close to 2.0 (2.38 and 2.06, respectively), indicating that the two-photon absorption process can occur in **Rh-NO-P** before and after the reaction with NO (as shown in Fig. 1e and f). We also investigated the quantum yield and two-photon activity cross-section of **Rh-NO-P** before and after the reaction with NO (see the ESI, Fig. S7 and Table S2†). It can be seen that the quantum yields before and after the reaction between **Rh-NO-P** and NO are 0.41 and 0.56, respectively, and the two-photon maximum activity cross-section at 800 nm reaches 49.5 GM and 189.8 GM, respectively, indicating that the probe can be applied for two-photon confocal imaging.

Based on the above findings, this study explored the response of the probe **Rh-NO-P** to the concentration of NO. The absorption spectra show that with the increase of the concentration of NO, the absorption peak at 350 nm is slightly increased while the absorption peak at 560 nm is significantly enhanced (shown in Fig. 2a). It can also be seen that the emission peak intensity at 611 nm gradually increases. Meanwhile, the fluorescence intensity at 457 nm gradually decreases (as shown in Fig. 2b), and the distance between the two emission peaks reaches 154 nm, indicating that the probe **Rh-NO-P** has a significant ratio response to NO. Besides, the two emission peaks have almost none of the crosstalk, thereby increasing the accuracy and resolution of the detection. We also investigated the relationship curve between the fluorescence intensity ratio ( $I_{611}/I_{457}$ ) and NO concentration. As shown in Fig. 2c and d, when the NO concentration is lower than 12  $\mu\text{M}$ , the  $I_{611}/I_{457}$  and NO concentration have a good linear relationship, and then the reaction reaches a plateau. The correlation coefficient  $R^2 = 0.994$ , indicating that the probe can achieve accurate detection of NO. More importantly, the detection limit of this method can be calculated as 51.3 nM based on  $\text{LOD} = 3\sigma/k$ . In addition, the reaction between **Rh-NO-P** and NO gradually reached a plateau after 20 s (red line in Fig. 2e), indicating that the probe **Rh-NO-P** can quickly respond to NO. In the absence of NO, no changes in  $I_{611}/I_{457}$  were observed in the reaction solution, indicating that the probe was stable in the system. The



**Fig. 2** (a) Absorption and (b) emission spectra for Rh-NO-P (10  $\mu\text{M}$ ) upon addition of NO (0, 0.5, 1, 2, 3, 4, 6, 8, 10, 12 and 14  $\mu\text{M}$ ). (c) Calibration curve and (d) linear correlation between the F.I. ratio ( $I_{611}/I_{457}$ ) of Rh-NO-P and the concentration of NO. (e)  $I_{611}/I_{457}$  of Rh-NO-P as a function of time after the addition of 12  $\mu\text{M}$  NO. PBS buffer solution (10 mM, pH 7.4, containing 10% DMSO). (f)  $I_{611}/I_{457}$  of Rh-NO-P for blank, Cys (1 mM), Hcy (1 mM), GSH (1 mM),  $\text{H}_2\text{O}_2$  (1 mM),  $\cdot\text{OH}$  (100  $\mu\text{M}$ ),  $\text{O}_2^{\cdot-}$  (100  $\mu\text{M}$ ), HOCl (100  $\mu\text{M}$ ),  $\text{NO}_2$  (100  $\mu\text{M}$ ),  $\text{ONOO}^-$  (100  $\mu\text{M}$ ),  $\text{NO}_2^-$  (100  $\mu\text{M}$ ),  $\text{SO}_2$  (100  $\mu\text{M}$ ),  $\text{H}_2\text{S}$  (1 mM),  $\text{H}_2\text{S}_n$  (1 mM),  $\text{Fe}^{3+}$  (1 mM),  $\text{Ca}^{2+}$  (1 mM),  $\text{Mg}^{2+}$  (1 mM),  $\text{Zn}^{2+}$  (1 mM),  $\text{Cu}^{2+}$  (1 mM), and NO (12  $\mu\text{M}$ ). One-photon excitation wavelength: 380 nm. In (c)–(f), data represent the mean of three replicates and the error bars indicate the SD. Concentration of Rh-NO-P: 10  $\mu\text{M}$ .

changes of  $I_{611}/I_{457}$  with the pH value of the solution before (green line) and after (red line) the reaction between the probe Rh-NO-P and NO (see the ESI, Fig. S8<sup>†</sup>). It can be seen that the

$I_{611}/I_{457}$  value of the probe Rh-NO-P in PBS solutions with different pH values (2–11) is basically unchanged, indicating that its fluorescence intensity before and after the reaction is

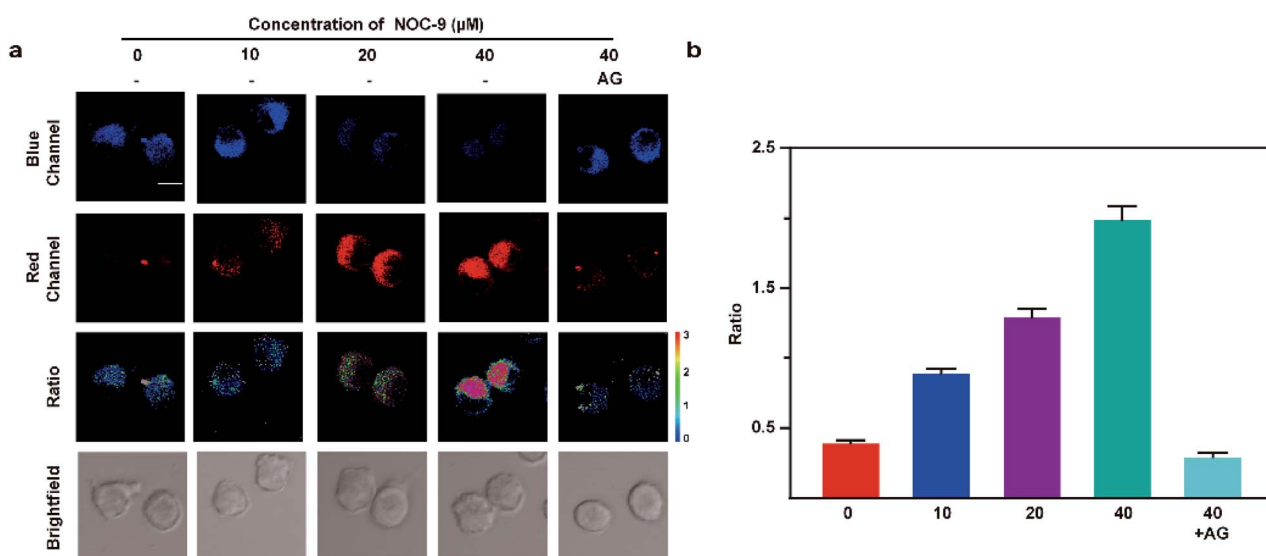


**Fig. 3** (a) Two-photon fluorescence images of BV-2 cells incubated with Rh-NO-P, obtained under different concentrations of NOC-9 (0, 10, 20, 40  $\mu\text{M}$ ) and 40  $\mu\text{M}$  NOC-9 pretreated with AG (0.5 mM). (b) Mean intensity ratio of (a). Emissions were collected at blue channel (410–530 nm) and red channel (580–650 nm) with 800 nm excitation. Scale bar: 50  $\mu\text{m}$ . Data represent the mean of three replicates and the error bars indicate the SD ( $n = 18$  cells from three independent cultures for each group).



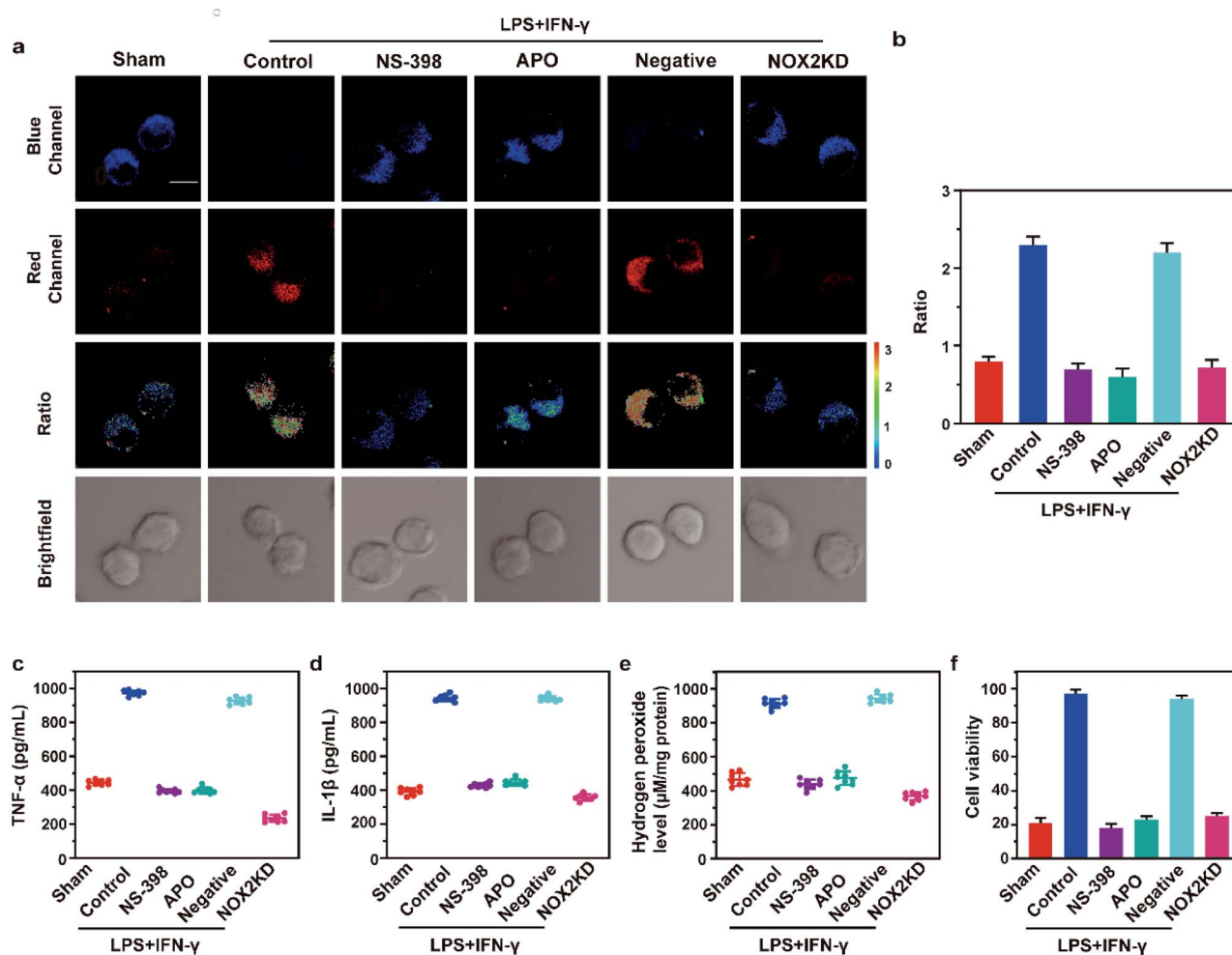


**Fig. 4** (a) Two-photon fluorescence imaging and (b) averaged fluorescence changes of Rh-NO-P-loaded (10  $\mu$ M) BV-2 cells when subjected to different treatments during LPS/IFN- $\gamma$  induced inflammation: Sham group (untreated cells); control group (LPS/IFN- $\gamma$  treated cells); NS-398 group (NS-398 treated cells during LPS/IFN- $\gamma$ -induced inflammation); APO group (APO treated cells during LPS/IFN- $\gamma$ -induced inflammation); negative group (negative control group of NOX2KD); and NOX2 KD group (NADPH oxidase 2 gene knockout). For the fluorescent images, the experiment was repeated using three cultures; similar results were obtained each time. Scale bar: 50  $\mu$ m. For changes in fluorescence: untreated cells, Sham group:  $n = 48$  cells from three cultures; LPS/IFN- $\gamma$  treated cells, control group:  $n = 61$  cells from three cultures; NS-398 treated cells during LPS/IFN- $\gamma$ -induced inflammation, NS-398 group:  $n = 51$  cells from three cultures; APO treated cells during LPS/IFN- $\gamma$ -induced inflammation, APO group:  $n = 51$  cells from three cultures; negative control group of NOX2KD, negative group:  $n = 65$  cells from three cultures; NADPH oxidase 2 gene knockout, NOX2KD group:  $n = 55$  cells from three cultures. ELISA of (c) TNF- $\alpha$  and (d) IL-1 $\beta$  levels in cells from samples shown in (a). (e) H<sub>2</sub>O<sub>2</sub> levels in cells from samples in (a). (f) CCK-8 analysis changes in cells from samples in (a). Emissions were collected at blue channel (410–530 nm) and red channel (580–650 nm) with 800 nm excitation. Scale bar: 50  $\mu$ m. In (b)–(f), the error bars indicate the SD.

basically not affected by the pH value. Finally, we investigated the selectivity of probe **Rh-NO-P** for NO. Interferents including Cys, Hcy, GSH, H<sub>2</sub>O<sub>2</sub>,  $\cdot$ OH, O<sub>2</sub> $\cdot^-$ , HOCl, NO<sub>2</sub> $^-$ , ONOO $^-$ , NO<sub>2</sub>, SO<sub>2</sub>, H<sub>2</sub>S, H<sub>2</sub>S<sub>n</sub>, Fe<sup>3+</sup>, Ca<sup>2+</sup>, Mg<sup>2+</sup>, Zn<sup>2+</sup>, and Cu<sup>2+</sup> were selected, and the fluorescence response of the probe was examined. It was found that  $I_{611}/I_{457}$  could not be significantly enhanced by interferents; however, it was enhanced after the addition of NO (Fig. 2f). These results indicate that the probe **Rh-NO-P** is highly selective for NO.

#### Bioimaging application of Rh-NO-P in living cells

In order to investigate whether the probe is suitable for cell imaging, its cytotoxicity was firstly detected. As shown in

Fig. S9,<sup>†</sup> the cell survival rate obtained by **Rh-NO-P** (0, 5, 10, 20, 30  $\mu$ M) cytotoxicity measurement with the MTT method is significantly higher than 85%, indicating that **Rh-NO-P** has low cytotoxicity and is suitable for cell imaging. Next, we conducted the light stability experiment of **Rh-NO-P** under a two-photon confocal microscope, and the results are shown in Fig. S10.<sup>†</sup> The cells were continuously excited with an 800 nm light source for 60 min, and the fluorescence intensity values at four locations a, b, c, and d were recorded regularly. Within 60 min, the fluorescence intensity of the probe after the reaction with NO does not fluctuate significantly, indicating that **Rh-NO-P** has good photostability and is suitable for long-term cell imaging.

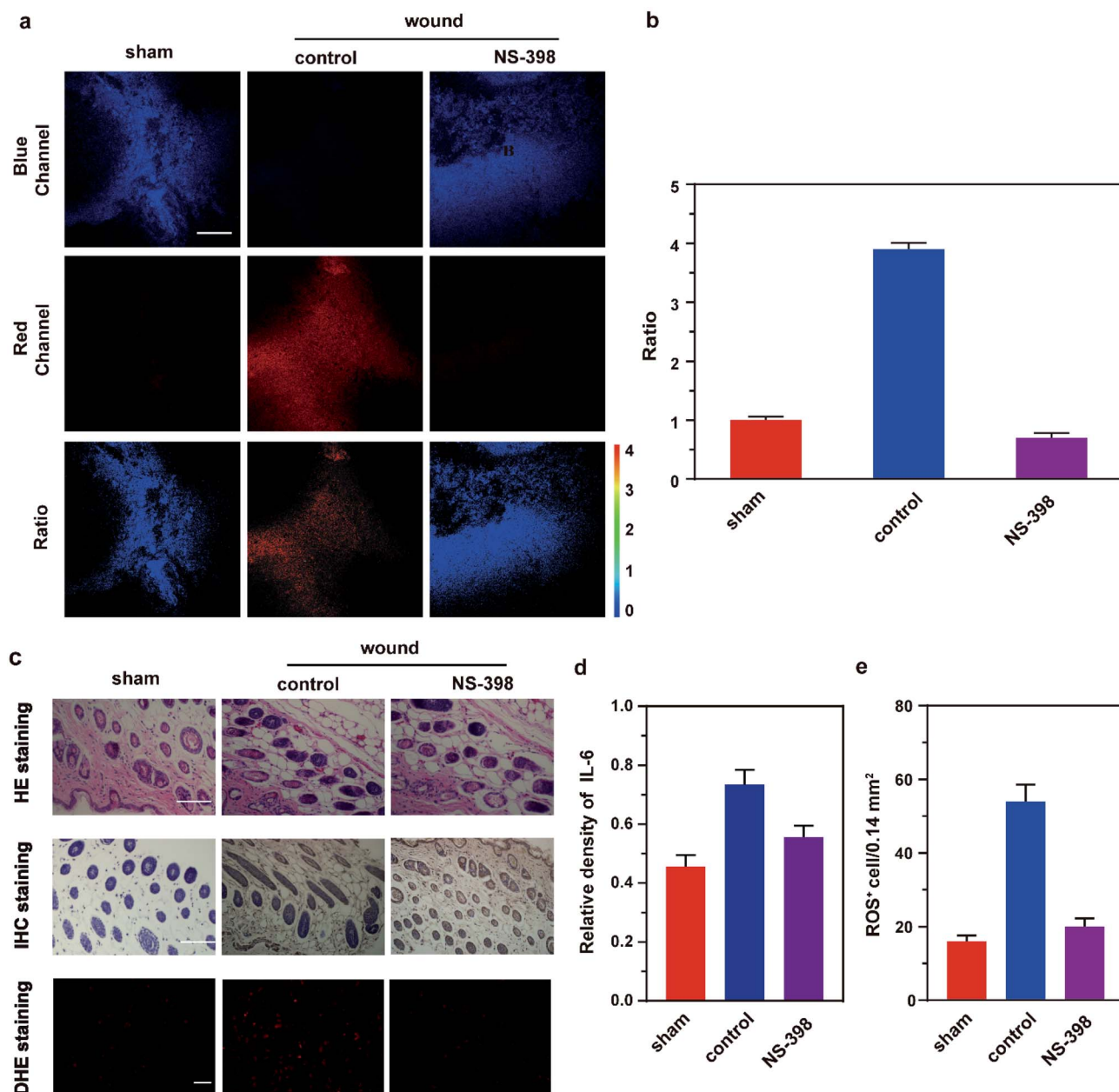


Fig. 5 (a) *In situ* TP fluorescence imaging of the wound healing tissue of mice and (b) averaged fluorescence intensity changes of Rh-NO-P-loaded (200  $\mu$ L, 100  $\mu$ M) wound healing tissue when subjected to different treatments: Sham group (untreated); control group (wound tissue) and NS-398 group (wound tissue pre-treated with NS-398). Emissions were collected at blue channel (410–530 nm) and red channel (580–650 nm) with 800 nm excitation. (c) Hematoxylin and eosin (H&E) staining (organ damage) analysis, IL-6 immunohistochemistry staining (IL-6 expression revealed) and DHE staining (ROS revealed) of wound tissue when subjected to different treatments. (d) and (e) Quantification of IL-6 and ROS-positive cells from samples shown in (a).  $n = 5$ /group. Scale bars: 200  $\mu$ m. In (b) and (d), (e), the error bars indicate the SD.

Then, the confocal imaging of Rh-NO-P for exogenous NO in BV-2 cells was conducted to explore the application of Rh-NO-P in living cells. The results are shown in Fig. 3. In two-photon confocal imaging, BV-2 cells were incubated for 30 min with NOC-9 with different concentrations (0, 10, 20, 40  $\mu$ M) and then were incubated for 20 min with 10  $\mu$ M Rh-NO-P. As the concentration of NOC-9 increased, the fluorescence of the blue channel (410–530 nm) of Rh-NO-P decreased continuously, while the fluorescence of the red channel (580–650 nm)

increased continuously. After the addition of 40  $\mu$ M NOC-9 and aminoguanidine AG (0.5 mM, NO scavenger), the fluorescence of the red channel disappeared, and the fluorescence of the blue channel was restored. The one-photon fluorescence imaging results are consistent with the two-photon fluorescence imaging results (Fig. S11<sup>†</sup>). These results indicate that the probe Rh-NO-P was able to detect exogenous NO with high sensitivity in either one-photon mode or two-photon mode.

Subsequently, in this work, we used LPS/IFN- $\gamma$  to stimulate the inflammatory response of cells. The overexpression of inducible nitric oxide synthase (iNOS) during the inflammatory response of cells resulted in the increase of NO levels. The two-photon fluorescence imaging results are shown in Fig. 4a and b. After the cells were treated with LPS and IFN- $\gamma$ , the fluorescence intensity of the red channel was significantly increased compared with that of the Sham group, while the fluorescence intensity of the blue channel was almost negligible. Inflammation inhibitor (NS-398), oxidative stress inhibitor (Apocynin, APO), and NOX-2 (ROS synthesis protein) gene silencing (NOX-2KD) were applied, respectively. The results showed that NO level was dramatically decreased, indicating that during the LPS/IFN- $\gamma$  stimulation, inflammation was caused by oxidative stress of cells. Besides, the ratio signal of the negative control group was significantly higher than that of the NOX-2KD group. The one-photon fluorescence imaging results are consistent with the two-photon fluorescence imaging results (Fig. S12<sup>†</sup>). The above experiments demonstrated that NOX-2 protein could regulate oxidative stress of cells and cause inflammation, whether in one-photon mode or two-photon mode. ELISA also demonstrated the accuracy of our view (Fig. 4c–e). The levels of the inflammatory factors TNF- $\alpha$  and IL-1 $\beta$ , and hydrogen peroxide (H<sub>2</sub>O<sub>2</sub>, a marker of cellular oxidative stress) had the same changing trend with the ratio signals, indicating that inhibiting oxidative stress could significantly suppress cellular inflammation. More importantly, the CCK-8 experiment showed that oxidative stress inhibitors and inflammation inhibitors could both alleviate cell death induced by cell inflammation. This conclusion provides a theoretical basis for wound healing in mice (shown in Fig. 4f).

### Bioimaging application of Rh-NO-P in wound healing tissues

Finally, we used fluorescence imaging of Rh-NO-P in tissues to conduct the in-site tracking of the NO fluctuation during wound healing in mice. Before that, we examined the tissue toxicity of Rh-NO-P. The hematoxylin and eosin (H&E) staining results of tissues at different sites show that there is no significant tissue damage after the addition of Rh-NO-P, indicating that the probe has small toxicity and is basically unharmed to the tissues (see the ESI, Fig. S13<sup>†</sup>). Besides, the imaging depth of Rh-NO-P in the tissues was derived by the Z-scan technique (see the ESI, Fig. S14<sup>†</sup>). The imaging depth of Rh-NO-P can reach 180  $\mu$ m, which proves that Rh-NO-P can be used for deep-skin tissue fluorescence imaging.

Based on the above findings, fluorescence imaging of inflammatory wound tissue of Rh-NO-P was investigated (Fig. 5). The mice were divided into three groups: the first group is the control group; the right feet of the mice in the second group were cut; the right feet of the mice in the third group were also cut, and the mice in the third group were given a subcutaneous injection of NS-398 through the inner thigh. 12 h later, the three groups of mice were injected subcutaneously with Rh-NO-P (200  $\mu$ L, 100  $\mu$ M) through the inner thighs. 1 h later, the wound biopsies of the three groups were imaged. The results were similar to those of the cell model. The red channel

fluorescence intensity of the skin tissue of mice in the wound group was significantly increased compared with that in the normal group, the blue channel fluorescence was negligible, and the ratio signal was significantly increased. The ratio signal of the NS-398 pre-injection group was significantly reduced compared with that of the wound group, indicating that the wound can induce inflammation in mice (Fig. 5a and b). H&E staining light microscopy showed that the mice in the control group had clear skin tissue structure and normal cell morphology while the mice in the wound group showed significant abnormalities in the skin tissue structure, with a significant increase in nuclear pyknosis. However, after adding NS-398, the tissue structure of mice was less damaged and recovered from time to time. The nuclear pyknosis was reduced, and inflammatory cells were reduced. Additionally, the expression of IL-6 by immunohistochemical staining analysis and ROS expression by DHE staining were consistent with the cellular results (Fig. 5c–e). The above experimental results show that the inflammation in mice is attributed to the wound, and NS-398 can protect the mice from skin damage caused by the inflammatory response.

## Conclusions

In this paper, based on the two luminescence mechanisms of the ESIPT effect and rhodamine open loop, a ratiometric two-photon NO fluorescent probe Rh-NO-P was designed and synthesized. This probe can recognize NO with high selectivity, and its maximum emission wavelength before and after response increased by 154 nm. There was almost no interference between the two emission peaks. When NO concentration was 0–12  $\mu$ M, there was good linearity, the response time was short ( $\leq 20$  s), the sensitivity was high, and the detection limit reached 51.3 nM. Additionally, the probe has low cytotoxicity and high biocompatibility. Confocal imaging shows that Rh-NO-P can achieve *in situ* imaging analysis of NO fluctuations in cells. The probe was successfully applied to monitor the changes of NO content in wound inflammation model tissues. The results show that mouse wounds can induce cell inflammation through oxidative stress and cause cell death. The use of oxidative stress inhibitors or inflammation inhibitors can inhibit cell death and ensure wound healing.

## Conflicts of interest

The authors declare no competing financial interest.

## Acknowledgements

This work was financially supported by the National Natural Science Foundation of China (No. 22166017), the Open Foundation of Hubei Key Laboratory of Biological Resources Protection and Utilization (PT012003), and Special Funds for “Double First-Class” Construction in Hubei Province, China. All animal procedures were performed in accordance with the Guidelines for Care and Use of Laboratory Animals of South-central University for Nationalities and experiments were

approved by the Animal Ethics Committee of College of Biology (South-central University for Nationalities).

## References

- 1 J. Zhang, A. Qian, L. Wei, C. Li, H. Wei, Y. Wang, S. Su, Y. He, C. Li and D. Sun, *Sens. Actuators, B*, 2021, **345**, 130329.
- 2 X. Zhu, J. Chen, C. Ma, X. Liu, X. Cao and H. Zhang, *Analyst*, 2017, **142**, 4623–4628.
- 3 H. Yu, Y. Xiao and L. Jin, *J. Am. Chem. Soc.*, 2012, **134**, 17486–17489.
- 4 P. R. Escamilla, Y. M. Shen, Q. Zhang, D. S. Hernandez, C. J. Howard, X. Qian, D. Y. Filonov, A. V. Kinev, J. B. Shear, E. V. Anslyn and Y. Yang, *Chem. Sci.*, 2020, **11**, 1394–1403.
- 5 Z. Mao, H. Jiang, Z. Li, C. Zhong, W. Zhang and Z. Liu, *Chem. Sci.*, 2017, **8**, 4533.
- 6 W. Hu, L. Zeng, S. Zhai, C. Li, W. Feng, Y. Feng and Z. Liu, *Biomaterials*, 2020, **241**, 119910.
- 7 C. Geraghty, C. Wynne and R. B. P. Elmes, *Chem. Rev.*, 2021, **437**, 213713.
- 8 T. Liang, T. Qiang, L. Ren, B. Wang and W. Hu, *Analyst*, 2021, **146**, 4659–4665.
- 9 T. Liang, D. Zhang, W. Hu, C. Tian, L. Zeng, T. Wu, D. Lei, T. Qiang, X. Yang and X. Sun, *Talanta*, 2021, **235**, 122719.
- 10 F. Cheng, T. Qiang, L. Ren, T. Liang, X. Gao, B. Wang and W. Hu, *Analyst*, 2021, **146**, 2632–2637.
- 11 Y. Liu, H. Fan, Y. Wen, T. Jia, Q. Su and F. Li, *Dyes Pigm.*, 2019, **166**, 211–216.
- 12 A. Loas and S. J. Lippard, *J. Mater. Chem. B*, 2017, **5**, 8929–8933.
- 13 M. Y. Lucero, A. K. East, C. J. Reinhardt, A. C. Sedgwick, S. Su, M. C. Lee and J. Chan, *J. Am. Chem. Soc.*, 2021, **143**, 7196–7202.
- 14 Z. Mao, H. Jiang, X. Song, W. Hu and Z. Liu, *Anal. Chem.*, 2017, **89**, 9620–9624.
- 15 H. Deka, S. Ghosh, S. Saha, K. Gogoi and B. Mondal, *Dalton Trans.*, 2016, **45**, 10979–10988.
- 16 Y. Zhang, C. Jia, Y. Wang, H. Yu and M. Ji, *Dyes Pigm.*, 2021, **197**, 109871.
- 17 W. Jiang, Y. Li, H. Liu, D. Zhou, J. Ou-Yang, L. Yi and C. Li, *Talanta*, 2019, **197**, 436–443.
- 18 Y. Fu, H. Li, X. Wei and Q. Song, *J. Mater. Chem. B*, 2019, **7**, 3792–3795.
- 19 Q. Wang, X. Jiao, C. Liu, S. He, L. Zhao and X. Zeng, *J. Mater. Chem. B*, 2018, **6**, 4096–4103.
- 20 S. J. Kim, S. Y. Park, S. A. Yoon, C. Kim, C. Kang and M. H. Lee, *Anal. Chem.*, 2021, **93**, 4391–4397.
- 21 H. Xiao, Y. Dong, J. Zhou, Z. Zhou, X. Wu, R. Wang, Z. Miao, Y. Liu and S. Zhuo, *Analyst*, 2019, **144**, 3422–3427.
- 22 S. Chen, B. Vurusaner, S. Pena, C. T. Thu, L. K. Mahal, E. A. Fisher and J. W. Canary, *Anal. Chem.*, 2021, **93**, 10090–10098.
- 23 B. Gu, M. Liu, C. Dai, Z. Zhou, D. Tang, S. Tang, Y. Shen and H. Li, *Sens. Actuators, B*, 2021, **344**, 130246.
- 24 L. Wang, J. Wang, S. Xia, X. Wang, Y. Yu, H. Zhou and H. Liu, *Talanta*, 2020, **219**, 121296.
- 25 S. H. Park, N. Kwon, J. H. Lee, J. Yoon and I. Shin, *Chem. Sci. Rev.*, 2020, **49**, 143–179.
- 26 M. Lv, Y. Zhang, J. Fan, Y. Yang, S. Chen, G. Liang and S. Zhang, *Analyst*, 2020, **145**, 7985–7992.
- 27 H. Yu, L. Jin, Y. Dai, H. Li and Y. Xiao, *New J. Chem.*, 2013, **37**, 1688–1691.
- 28 L. Zhao, Z. Huang, D. Ma, Y. Yan, X. Zhang and Y. Xiao, *Analyst*, 2021, **146**, 4130–4134.
- 29 P. Yue, X. Yang, P. Ning, X. Xi, H. Yu, Y. Feng, R. Shao and X. Meng, *Talanta*, 2018, **178**, 24–30.
- 30 P. Jia, Z. Zhuang, C. Liu, Z. Wang, Q. Duan, Z. Li, H. Zhu, F. Zhang, W. Sheng and B. Zhu, *Dyes Pigm.*, 2020, **173**, 107942.
- 31 L. He, X. Yang, K. Xu and W. Lin, *Anal. Chem.*, 2017, **89**, 9567–9573.
- 32 X. Song, C. Li, Y. Wang, D. Wang and Z. Liu, *Sens. Actuators, B*, 2020, **311**, 127895.
- 33 M. Beija, C. A. M. Afonso and J. M. G. Martinho, *Chem. Sci. Rev.*, 2009, **38**, 2410–2433.
- 34 X. Li, Y. Yin, J. Deng, H. Zhong, J. Tang, Z. Chen, L. Yang and L. Ma, *Talanta*, 2016, **154**, 329–334.
- 35 Y. M. Poronik, K. V. Vygranenko, D. Gryko and D. T. Gryko, *Chem. Sci. Rev.*, 2019, **48**, 5242–5265.
- 36 J. Zhu and K. M. C. Wong, *Sens. Actuators, B*, 2018, **267**, 208–215.
- 37 H. Wang, J. P. Guan, X. Han, S. W. Chen, T. B. Li, Y. R. Zhang, M. S. Yuan and J. Y. Wang, *Talanta*, 2018, **189**, 39–44.